Quantitative Coronary Angiography with Deformable Spline Models

Andreas K. Klein, Forester Lee, and Amir A. Amini,* *Senior Member, IEEE*

***Abstract*— Although current edge-following schemes can be very efficient in determining coronary boundaries, they may fail when the feature to be followed is disconnected (and the scheme is unable to bridge the discontinuity) or branch points exist where the best path to follow is indeterminate. In this paper, we present new deformable spline algorithms for determining vessel boundaries, and enhancing their centerline features. A bank of even and odd S-Gabor filter pairs of different orientations are convolved with vascular images in order to create an external snake energy field. Each filter pair will give maximum response to the segment of vessel having the same orientation as the filters. The resulting responses across filters of different orientations are combined to create an external energy field for snake optimization. Vessels are represented by B-Spline snakes, and are optimized on filter outputs with dynamic programming. The points of minimal constriction and the percent-diameter stenosis are determined from a computed vessel centerline. The system has been statistically validated using fixed stenosis and flexible-tube phantoms. It has also been validated on 20 coronary lesions with two independent operators, and has been tested for interoperator and intraoperator variability and reproducibility. The system has been found to be specially robust in complex images involving vessel branchings and incomplete contrast filling.**

***Index Terms*— B-spline snakes, coronary angiography, deformable models, dynamic programming, Gabor filters.**

I. Introduction

CORONARY artery disease (CAD) causes in excess of 1.5 million cases of myocardial infarction annually, and is the leading cause of death in the United States, resulting in more than 500 000 deaths per year [43]. The accurate diagnosis and quantification of CAD is critical to subsequent treatment decisions, such as whether the patient should pursue pharmacological treatment, other nonsurgical treatment such as angioplasty, or bypass surgery.

A. Coronary Angiography

Direct visual examination of cine film coronary angiograms and manual estimation of the degree of vascular stenosis were the unblemished "gold standard" examination of vascular pathology until the mid 1980's [48]; and they remain the standard in clinical practice today [9], [33]. Beginning in the mid 1970's [14], [52] concerns were raised regarding the accuracy and variability of measurement obtained subjectively through manual reading, motivated by several factors. First, as the basis for the standard of clinical practice, visual interpretation needed some description of it's appropriateness. While angiographic findings were being used daily to make vital patient care decisions regarding prognosis, treatment, and disease progression, no studies had tested the assumptions that vessel geometries by visual estimation were valid markers for measuring the extent of CAD [43]. Studies attempting to follow the slow, incremental progression of atherosclerotic disease were complicated by the excessive variability and insufficient accuracy in manual judgment. Changes in vessel dimensions over time resulting from progression of CAD were smaller than could be reliably be measured visually [16], [31]. Quantitative coronary angiography (QCA) has been developed to apply the speed and precision of computer processing to the analysis of coronary disease [50].

Angiography aims to indirectly measure the reduction in oxygenating capacity of the coronary vasculature from the vessel dimensions [20]–[23]. There are several technical limitations which must be considered for their impact in subsequent analyzes of vascular pathology [36]–[38], [45]. These include incomplete contrast filling of the vessels; vessel dilation proximal to an obstruction and vasoconstriction along the entire vessel, both resulting from the introduction of contrast; penumbra effect (blurring of vessel edges in the image due to the finite width of the x-ray beam; magnification of the vessel dimensions due to the diverging x-ray beam; and, finally, pincushion distortion resulting from electronic limitations.

B. QCA System Goals

Historically, studies have shown a statistically significant correlation between the absolute measures of minimum diameter and minimum area, and physiological effect [15], [18], [19], [25]. More recent studies, using QCA, have also been able to show a significant correlation between the percent stenosis measures and physiological effect [49].

In order to assess the clinical utility of any QCA system, a set of minimum capabilities for any system must be defined. These minimum capabilities serve as a basis for assessing different approaches and may serve to identify targets for system improvement. Performance benchmarks for accuracy and precision can be determined based on angiographic follow-up

Manuscript received August 21, 1995; revised December 17, 1996. This work was supported in part by a grant from the Whitaker Biomedical Engineering Foundation. The work of A. A. Amini was supported by the National Science Foundation under Grant IRI-9796207. The Associate Editor responsible for coordinating the review of this paper and recommending its publication was N. Ezquerra. *Asterisk indicates corresponding author.*

A. K. Klein is with the Department of Internal Medicine, New England Medical Center, Boston, MA 02111 USA.

F. Lee is with the Department of Cardiology, Yale University School of Medicine New Haven, CT 06520 USA.

*A. A. Amini is with the Cardiovascular Image Analysis Lab, Box 8220, Washington University Medical Center, 216 S. Kingshighway, St. Louis, MO 63110 USA (e-mail: amini@mobius.wustl.edu).

Publisher Item Identifier S 0278-0062(97)07890-7.

studies measuring the progression of disease, as well as physiologic experiments measuring the decline of vessel response to a vasodilatory stimulus, i.e., coronary flow reserve (CFR) [20]. These studies provide evidence for the expected magnitudes of the vessel dimensions or incremental changes in dimensions.

Several studies have established tolerances for the accuracy and precision of quantitative angiographic systems based on clinical data. Rensing *et al.* [40] studied 350 patients with single-vessel coronary artery disease who had undergone balloon angioplasty. They compared functional status (recurrent angina and/or electrocardiogram (EKG) changes with exercise) with the results of angiography at six month follow up. Any one of the following was found to have the highest accuracy in predicting anginal status: minimal lumen diameter of 1.45 mm (the vessels studied had a median reference diameter of 2.63 mm), percent-diameter stenosis of 45.5%, an interval luminal narrowing of 0.30 mm, and an interval change in percent-diameter stenosis of 10%. Essentially identical results were found for the prediction of exercise tolerance.

Wilson *et al.* examined the CFR of 50 patients with a single vessel lesion by the administration of a potent vasodilator via coronary angiographic catheter [49]. The resting and maximal blood flow past the lesion were recorded with a Doppler catheter. A minimum luminal area of less than 2.5 mm^2, percent-area stenosis greater than 70%, and percent-diameter stenosis greater than 60% correlated with a physiologically significant decrease in the coronary flow reserve. A minimum luminal area of 2.5 mm^2 corresponds to a minimum diameter less than 0.9 mm.

Both of these studies establish the minimum digital quantitative angiography (DQA) system requirements from a clinical perspective. In order to predict accurately functional status, any DQA system must be capable of accurately measuring stenoses on the order of 1.4 mm with a resolution better than 0.3 mm required to evaluate interval changes. Thus precisions (which reflect repeatability of the system and the spread of possible errors) must be less than 0.3 mm to detect interval change. In order to predict functional impairment even at a sub clinical level, it must be able to accurately measure absolute luminal diameters down to less than 0.9 mm. Any new DQA system should meet these minimal criteria.

C. Current Limitations

As advanced as the automated QCA systems have become, they remain limited in their variability by virtue of requiring operator input in order to "find" the vessel to be measured. These systems are sensitive to the initial conditions imposed by the operator. Some researchers have gone to great lengths to reduce the dependence on initial conditions, notably Reiber *et al.* [39] require only a beginning and end point of the rough fit centerline. The system then tracks the centerline in a low resolution version of the desired image and projects this estimate of the centerline back onto the original image. Interoperator variability is a direct consequence of system sensitivity to initial conditions.

The QCA systems of Reiber [39], Brown [5]–[7], Figueiredo [17], and van der Zwet [54] all use least-cost edge following to identify the vessel borders for subsequent analysis. Edge following schemes can be very efficient, but they may fail when the feature to be followed is disconnected (and the scheme is unable to bridge the discontinuity) or branch points exist where the best path to follow is indeterminate. In the analysis of coronary vasculatures, these situations may arise when there is incomplete contrast filling of vessels, where vessels branch, or when vessels at different depths appear to overlap one another.

Unfortunately, in the majority of cases, studies have selected vessels of simple geometry with discrete disease for system analysis, a situation which represents less than 30% of cases actually encountered in clinical practice [21]. Recently, Gurley *et al.*, explored operator- and patient-dependent factors which impacted the performance of a commercially available system (General Electric DCX-ADX, Schenectady, NY) [24]. They discovered that fully automatic border detection only worked on 20 of 38 lesions (from 25 consecutive patients) unanimously selected as stenoses by a panel of four angiographers. The 18 failures involved tracking over regions of complicated geometry: 72% involved a stenosis at vessel branch point, 44% involved an excessively tortuous vessel or overlap, 22% involved both tortuosity and overlap, and 28% involved poor image quality. Automatic border detection and vessel measurement failed in 52% of sequential clinical angiograms.

These two problems highlight the need for further improvement in QCA systems. In this paper, we describe a unique edge identification algorithm which robustly measures vessel geometry over a wide spectrum of vessel lesions from discrete to diffuse, and geometries from simple to complex. The system also aims to reduce the bias introduced by the operator with an eye toward eventual full automation of vessel boundary mapping.

II. Proposed Algorithm

A. Energy Minimizing Snakes

Energy minimizing splines, commonly called snakes, offer clear advantages over edge following methods as they incorporate both local image and expected contour information [28]. As was previously stated, edge following methods are prone to failure when the edges are disconnected or multiple alternate paths are present (at vessel overlaps or branches). These methods are vulnerable because they only utilize local image information; they do not incorporate any higher level information—such as the expected length or shape—which could guide the path over breaks or past indeterminate solutions. Snake algorithms are relatively tolerant of the local discontinuities in image intensity information and ambiguities in path which hamper other techniques.

Snakes are deformable curve models which lock onto nearby edges and accurately localize them. They are guided to their best fit conformation by a balance between external forces imposed on them by the image, and internal shape constraints which keep them smooth. Snakes have an associated energy function which can be written

$$\varepsilon_{\text{snake}} = \varepsilon_{\text{external}} + \varepsilon_{\text{internal}} \tag{1}$$

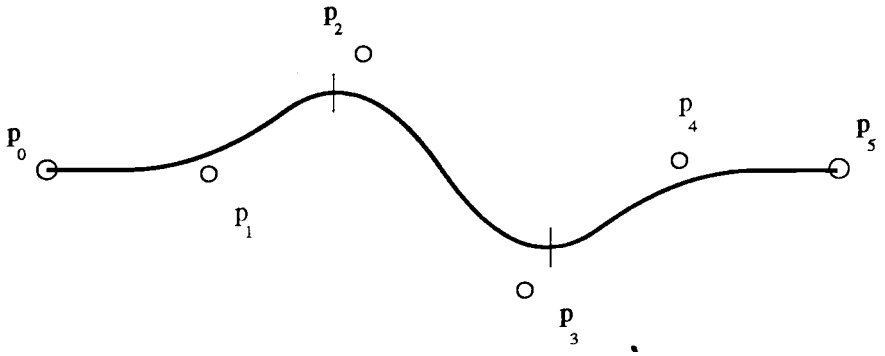

Fig. 1. Spanwise cubic B-spline with three spans (shown separated by vertical bars) and six control points. The first span is controlled by points p_0–p_3, the second by points p_1–p_4, and the last by points p_2–p_5.

$$= \int_0^l \varepsilon_{\text{image}}[v(s)]\,ds + \int_0^l \alpha|v_s(s)|^2 + \beta|v_{ss}(s)|^2\,ds \tag{2}$$

for a snake, $v(s)$, of length l. The total energy, $\varepsilon_{\text{snake}}$, reaches a minimum value as the snake locks onto a salient image contour. The snake energy, as originally proposed by Kass *et al.*, was the sum of an external energy

$$\varepsilon_{\text{image}}[v(s)] = -|\nabla I[\alpha(s)]|^2 \tag{3}$$

where ∇ is the local image gradient operator, and an internal energy derived from a combination of derivatives along the spline which enforced smoothness [28]. Snakes and other deformable boundary models have been used to track movement in magnetic resonance [1], [2] and X-ray [3], [10] images; and accurately locate neural dendrites in electron micrographs [8], facial features in photographs [51], and cardiac silhouettes in ultrasound images [44].

B. B-Spline Snakes

As the basis functions for energy maximizing snakes, B-splines have several characteristics which make them well suited to describing vessel contours as well as optimization using dynamic programming: 1) they are smooth,[1] continuous curves which are in general less dependent on internal energy constraints (and, hence, the additional weighting terms α and β in (2), 2) they are completely specified by few control points, and 3) individual movement of the control points will only affect them locally [2], [34] (Fig. 1). B-splines are given by the following expression:

$$v(u) = \mathbf{u}^{\mathrm{T}}\mathbf{M}\mathbf{P} \tag{4}$$

where $\mathbf{u}$ is a column vector of powers of u, the spline parameter, $\mathbf{P}$ is a sequence of control points, and $\mathbf{M}$ is a matrix which blends the control points. B-splines can be constructed of any order (with the complexity of the possible conformation increasing with spline order), but second- (quadric) and third-order (cubic) are most often encountered. Quadric and cubic B-splines exhibit a favorable tradeoff between their shape complexity for describing natural curves and computational burden required to solve them. To increase the shape complexity of the B-spline without dramatically increasing computational burden, any number of quadric or cubic B-spline segments can be strung together to create a piecewise quadric or cubic spline (Fig. 2).

To identify the edge features in the image, the following expression must be minimized along the B-spline curve

$$\varepsilon_{\text{snake}} = -\int_0^l \varepsilon[v(s)]\,ds \tag{5}$$

where $\varepsilon[v(s)]$ is appropriate image-derived information. The specific image-derived information in our QCA system is explained in Section II-D.

For a piecewise cubic B-spline, (5) may be written in the form

$$\varepsilon_{\text{snake}} = \varepsilon_0(p_0, p_1, p_2, p_3) + \varepsilon_1(p_1, p_2, p_3, p_4) + \cdots + \varepsilon_{N-4}(p_{N-4}, p_{N-3}, p_{N-2}, p_{N-1}) \tag{6}$$

where p_i are the B-spline control points, N is the total number of control points, and ε_n are the energies for each span. Note that as defined here, the shape and, thus, the energy, of each piecewise cubic span depends only on four adjacent control points. It would be possible to impose derivative smoothness penalties on the B-spline curve as in (2); however, for the application at hand, the derivative penalties are felt not to be needed. furthermore, the added smoothness penalties will require additional weight terms that will need to be adjusted, leading to variability in the results.

C. Dynamic Programming

Dynamic programming (DP) is a very efficient method for optimizing problems which can be broken down into a number of independent steps [1], and dramatically reduces the number of calculations over exhaustive enumeration. Given a cubic B-spline with N total control points and n possible positions for the N control points, the total number of possible solutions is n^N. However, the total number of steps needed to find the optimum solution by DP is $O(n^4N)$. Thus, for any number of control points greater than four, DP offers dramatic increases in efficiency. And, as more control points are added, the number of steps increases linearly; while the total number of possible solutions increases exponentially.

[1] Please note that although this is the case, one can create corners in such curves by placement of coincident knot points.

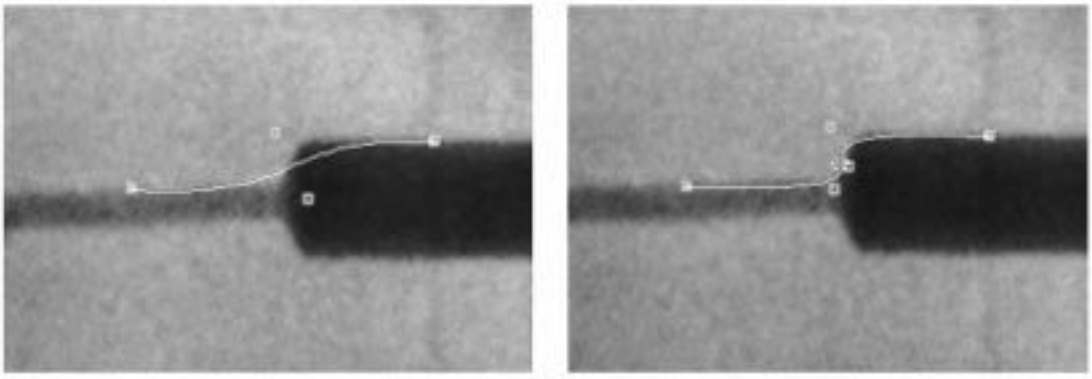

(a) (b)

Fig. 2. B-splines with (a) four control points and one span and (b) with five control points and two spans. This figure demonstrates the increase in complexity, needed to match image contours, which can be attained by increasing the number of piece wise cubic spans.

The QCA systems of Reiber and van der Zwet also employ DP [39], [47]. In the case of least-cost edge following of Reiber, the number of steps required to find the optimum solution is $O[(3)^2N]$ assuming a simple path constrained only by the last point found. In the case of the least-cost scheme presented by van der Zwet, the number of steps required is $O[(9)^2N]$. Note that both of these implementations depend heavily on the total length of the edge to be followed, N, since each point along the path can be considered an independently variable control point of a linear spline. As the edge length increases linearly, the number of steps to find the solution increases linearly. In contrast, the number of steps to solve the B-spline snake is independent of the actual length of the edge, since the same number of control points can be used to span any distance. Thus N, in the case of line following, is much greater in practice than in the case of B-spline snakes.

Dynamic programming may be used to optimize the continuous B-spline curve in the control point space to minimize $\varepsilon_{\text{total}}$ using the following recurrence:

$$S_i(p_i, p_{i+1}, p_{i+2}) = \min_{p_i - 1} \{ \varepsilon_{i-1}(p_{i-1}, p_i, p_{i+1}, p_{i+2}) + S_{i-1}(p_{i-1}, p_i, p_{i+1}) \} \quad (7)$$

for $i \geq 3$, and

$$S_1(p_1, p_2, p_3) = \min_{p_0} \{ \varepsilon_0(p_0, p_1, p_2, p_3) \}. \quad (8)$$

In general, for an order-k B-spline, S_i is a function of k control points [2]. This minimization yields the optimal open spline, as is the case for a vessel border. This algorithm is easily extended to include closed splines, which are useful for area and volume measurements.

In practical terms, the iterative optimization scheme for spanwise cubic B-spline snakes can be summarized as follows. Beginning with the first span, the locations of all four control points are varied systematically within a limited window and the energy corresponding to each conformation is calculated. These energies are minimized over the first control point. The procedure is repeated for the next span, the conformation of which is controlled by the last three control points of the previous span and the next control point in the sequence. Energies corresponding to all of the possible locations of these four control points are calculated from the spline energy plus the minimum energies from the first span. This scheme continues until all the control points have been varied, and the minima of all the remaining conformations can be sought. Stepping back through stored optimal control point locations reveals the lowest energy state conformation. This optimization process is repeated until the overall spline energy reaches a minimum; i.e., there is no lower energy state than the one occupied by the snake.

Iterative DP Algorithm for B-Spline Snakes:

1) Initialize B-Spline, $v(s)$ in the image.
2) Minimize $\varepsilon_{\text{snake}}[v^i(s)] \rightarrow \varepsilon_{\text{snake}}[v^{i+1}(s)]$ using (7) and (8).
3) For all j, update $\{p_j\}^i \rightarrow \{p_j\}^{i+1}$.
4) If $i >$ MAX or $|\varepsilon_{\text{snake}}[v^i(s)] - \varepsilon_{\text{snake}}[v^{i+1}(s)]| <$ THRESHOLD, then HALT.
5) $i = i + 1$.
6) Goto Step 2).

where i is the iteration index. Note that each control point is optimized within a $M \times M$ pixel window.

D. Image Filtering

1) Traditional Techniques: Both the least-cost algorithms and the snake algorithms use image intensity information to determine their optimal paths. Costs and energies may be derived from the image itself (i.e., image gradients, as have been traditionally used), or from enhanced images where the application of digital filtering techniques has increased the contrast between the features of interest and the background.

Many different methods for enhancing object edges in images have been used in computer vision applications, as well as in QCA systems described in the literature. Ellis *et al.* [16] apply a first derivative to the image intensity along scanlines drawn perpendicular to an initial, rough-fit centerline. However, this has been shown to result in underestimation of vessel width. Reiber [39], Mancini [32], and others combine first and second spatial derivatives along a similar series of centerline perpendiculars to locate potential vessel edges. The added requirement of the vessel centerline

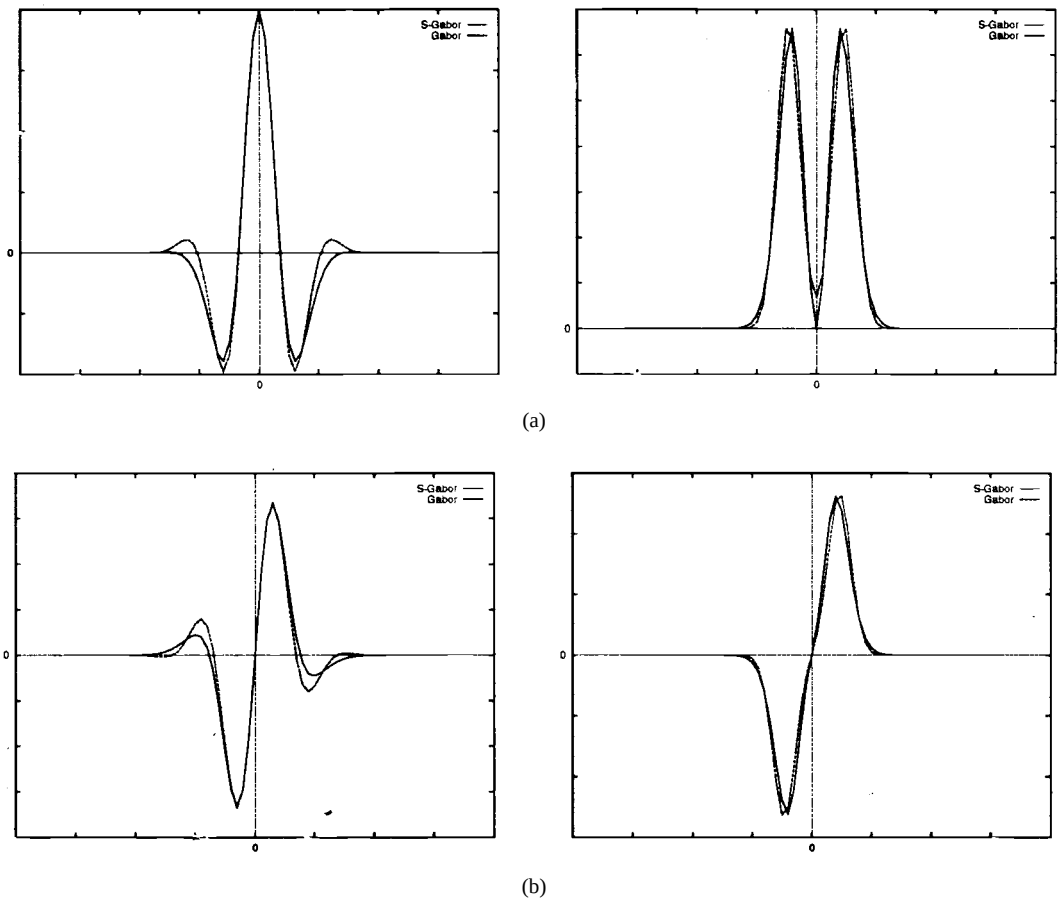

Fig. 3. (a) Even and (b) odd Gabor and S-Gabor functions and their Fourier transforms. Note that the magnitude of the Fourier transform of the even Gabor filter is nonzero at a frequency of zero, revealing the nonzero dc response of this filter. By comparison, the magnitude of the Fourier transform of the even S-Gabor filter is zero.

and the relative weights of the first and second derivatives (which must be determined empirically) can be potential drawbacks to these approaches.

Other digital filters used in computer vision for edge detection are more global in extent and include the derivative of gaussians (DOG) [42], laplacian of Gaussians (LOG) [35] and quadrature pair filters [30], [41]. These filters combine image information over a wide area (typically $>$100 pixels). Quadrature pair filters are gaining in popularity as they provide the most accurate models of natural vision systems, based on experimental data [11], [30].

2) Gabor Filters: Gabor filters belong to the family of quadrature pair filters [30]. They enhance line and edge features, are selective for orientation and frequency, and their outputs may be combined to produce a robust external energy term for snake optimization. Additionally, they have a number of advantages over the spatial derivative, DOG, and LOG edge enhancement schemes described earlier [12], [13]. The Gabor filters can be two-dimensional (2-D) filters and can be designed to enhance edges of any orientation. These filters do not require empirically weighted averaging functions to accurately locate edge features, and they accurately enhance *both* lines and edges. The Gabor-filter outputs are well suited to identifying vascular features and driving the optimization of snakes.

The one-dimensional (1-D) Gabor-filter pair is defined as follows [26]:

$$S(x) = e^{x^2/2\sigma^2} \cdot \sin[2\pi v_0 x] \tag{9}$$

$$C(x) = e^{x^2/2\sigma^2} \cdot \cos[2\pi v_0 x] \tag{10}$$

where x is the distance along the axis, σ determines the width of the Gaussian envelope and v_0 is the modulation frequency. $S(x)$ defines the odd, antisymmetric function and $C(x)$ defines the even, symmetric Gabor function. The 1-D Gabor filters can be extended to two dimensions by simply multiplying the 1-D Gabor functions by a Gaussian lowpass filter in the orthogonal direction [30].

3) S-Gabor Filters: Heitger *et al.* proposed an extension of Gabor filters to address the issue of nonzero dc response existing with the even Gabor filter by including a sweep to lower frequency in the sine and cosine functions [26]. The enhancement of small vessels and sharp edges of large vessels would be compromised by a nonzero dc filter. Their 1-D S-Gabor ("Stretched-Gabor") functions can be written

$$S(x) = e^{x^2/2\sigma^2} \cdot \sin[2\pi v_0 x \psi(x)] \tag{11}$$

$$C(x) = e^{x^2/2\sigma^2} \cdot \cos[2\pi v_0 x \psi(x)] \tag{12}$$

with

$$\psi(x) = k \cdot e^{-\lambda(x/\sigma)^2} \tag{13}$$

where k is the relative contribution of the frequency sweep and λ determines the rate of the frequency sweep. Heitger *et al.* further state that for a given k, σ, and v_0 with $\sigma * v_0 > 0.38$ there exists at least one λ which will satisfy the condition of zero dc, namely, that the integral over the length of the even filter is zero. The function $\psi(x)$ has the effect of increasing the wavelength of the sine and cosine functions with increasing distance from the origin, adding weight to the negative side lobes of the even filter. This adds sufficient negative area to make a zero integral solution possible (Fig. 3).

The 1-D S-Gabor filters can be extended to two dimensions by two separate methods. The first method extends the filters to two dimensions by multiplying the 1-D kernels with a Gaussian kernel in the y direction [30]. The effect of the Gaussian envelope oriented perpendicular to the major axis of the Gabor filter is one of averaging or summing the intensity information along the edge or line features to be enhanced. In this case, the orientation of the filter is set by application of a rotation matrix of the appropriate angle to the 2-D filter

$$S(x) = \exp\left[-\frac{1}{2}\left(\frac{x^2}{\sigma_x^2} + \frac{y^2}{\sigma_y^2}\right)\right] \cdot \sin\left[2\pi v_0 x \psi(x)\right] \quad (14)$$

$$C(x) = \exp\left[-\frac{1}{2}\left(\frac{x^2}{\sigma_x^2} + \frac{y^2}{\sigma_y^2}\right)\right] \cdot \cos\left[2\pi v_0 x \psi(x)\right] \quad (15)$$

$$\psi(x) = k \cdot e^{-\lambda(x/\sigma_x)^2}. \quad (16)$$

The choice of the widths of the Gaussian envelopes, σ_x and σ_y, determine the frequency and orientation selectivity of the 2-D S-Gabor filter, respectively. σ_y controls how long and continuous, as well as how closely oriented to the filter's major axis a feature must be to be enhanced. σ_x controls how sharp, or quickly arising from the background the edge or line must be to be enhanced. A ratio of $\sigma_x/\sigma_y = 0.55$ was derived by Kulikowski *et al.* from single cat striate cortical cell recordings [30].

A second method for extension of the S-Gabor filters to two dimensions was proposed by Heitger *et al.* which simultaneously enforces polar separability and sets the filter orientation [26]. This method involves constructing a polar 2-D operator in the Fourier domain by assigning the 1-D Fourier transform of the 1-D S-Gabor filter (which is a function of filter frequency only) to the radial variation, $\Re(r)$, and multiplying it by a power of a cosine function

$$\Im(r, \phi) = \Re(r) \cdot \cos^{2m}(\phi_0 - \phi) \quad (17)$$

where ϕ_0 sets the filter orientation, and m the sharpness of the orientation selectivity. This function in r and ϕ is then discretely sampled onto the Cartesian coordinate plane using bilinear interpolation. Taking the inverse Fourier transform of the Cartesian-sampled filter, then completes the construction of the 2-D filter.

E. Energy Field

The magnitude and direction of variations in image intensity describe line and edge features contained in an image. The intensity of the S-Gabor filtered image at each point may be used to drive an energy minimizing snake onto contours within the image. The energy field, E is defined as the vector magnitude of the filter outputs obtained by convolving the even and odd S-Gabor filters of orientation θ with the image, I

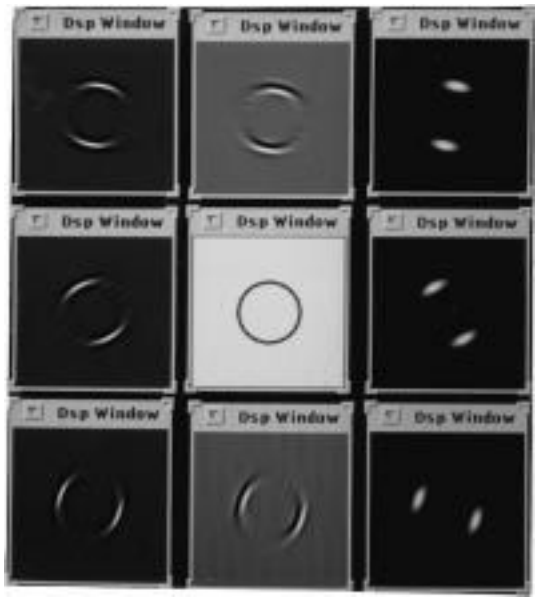

(a) (b) (c)

Fig. 4. Vector magnitude of the S-Gabor filter outputs at three different orientations for a synthetic circle. (a) The even filter response, (b) the odd filter response (except in the center where the original image has been substituted), and (c) the energy field.

$$E(\theta) = \sqrt{[C(\theta) * I]^2 + [S(\theta) * I]^2}. \quad (18)$$

This square law nonlinearity has been shown to exhibit a single peak response to edges, lines, and features combining elements of both. It should be noted that the location of the peak energy corresponds exactly to the location of these characteristic features. However, the *energy* conveys no information as to the particular type of feature which generated the response [26]. The *phase* conveys the character of the feature—whether it is more like a line or more like an edge

$$\Phi(\theta) = \tan^{-1}\left[\frac{S(\theta) * I}{C(\theta) * I}\right]. \quad (19)$$

To create an energy field of enhanced even and odd features of any orientation, a bank of filters at different orientations may be convolved with the image and the energy computed for each orientation. The maximum energy response across the bank of filters at each point in the image defines a composite energy field

$$\varepsilon(x, y) = \max_{\theta} E(x, y, \theta). \quad (20)$$

This results in a composite image of enhanced edge and line features of all orientations spanned by the range of θ in the bank of filters. The number and spacing of orientations within the bank depends on the orientation selectivity of the filter. The narrower the range of orientation selectivity, the more closely the filters will be need to be spaced in order to enhance all possible orientations. The energy field provides the external forces which pull the energy minimizing snake onto the image contours.

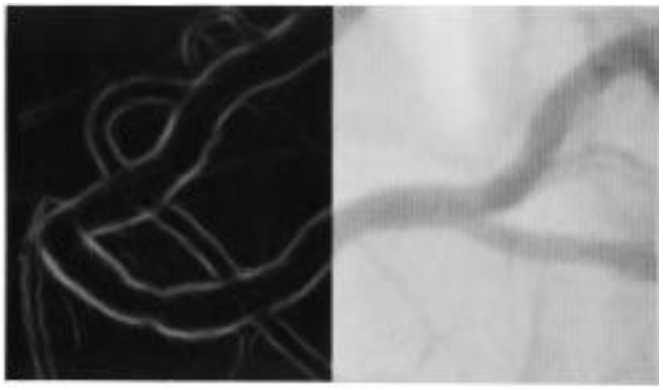

(a) (b)

Fig. 5. Energy field resulting from the convolution of a region of a clinical angiogram with a bank of 12 evenly spaced S-Gabor filters, each specific to a particular orientation.

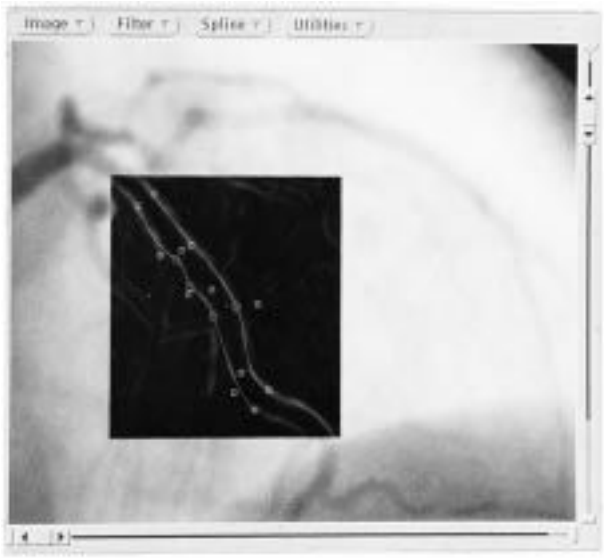

Fig. 6. Example screen of interactive image processing package developed to implement the S-Gabor filter and B-spline snake algorithm.

Fig. 4 displays the result of convolving S-Gabor filters with a synthetic image of a circle. In this figure, the output of the S-Gabor filter pairs in three different orientations can be viewed. Each of the images in Fig. 4 demonstrates edge enhancement which is selective for orientation: edge features oriented along the major axis are enhanced, while those away from this orientation are suppressed. The image in Fig. 5 is the energy field resulting from convolving the image with a bank of 12 evenly spaced S-Gabor filters and taking the maximum intensity across the bank at each point. The energy field contains edge features of all orientations, and reveals features suppressed in the single filter images.

F. Summary

The system proposed in this paper identifies vessel boundaries using energy minimizing snakes by integrating local image intensity information over a large spatial extent. These snakes use piecewise cubic B-splines as their basis functions, which efficiently and accurately describe natural contours such as those encountered in coronary angiography. Their piecewise continuous description of complex borders makes them well suited to optimization with the dynamic programming scheme described. To provide the external energy to drive the snakes onto the vessel boundaries, we have chosen to combine the outputs of a bank of S-Gabor filters. These filters are tuned to characteristic vessel dimensions, accurately enhance both lines and edges simultaneously, and are selective of feature orientation, capturing the tortuosity of blood vessels. The unique combination of described methods produces a powerful tool for accurate and robust identification of complex boundaries of vessels in coronary angiograms; a tool which is relatively insensitive to vessel intersections and branches which confound similar systems.

III. METHODS

A series of validation experiments was designed and carried out to determine the performance of the S-Gabor filter and DP B-spline snake vessel dimension measurement system. Parameters evaluated included the overall accuracy and precision of the system, and the ability of the system to robustly identify the vessel contours regardless of the initial snake placement. First, phantom studies were performed to measure system accuracy and precision under ideal conditions with a single operator. Splines before and after optimization were compared for overall fit. Next, the system was applied by two independent operators to a random sequential series of angiograms performed at the Yale-New Haven Hospital digital coronary catheterization lab, and precision was evaluated. The fit of the splines between runs for each operator were also compared.

An OpenWindows based imaging software package has been developed to implement the presented edge identification system (Fig. 6). All development and analysis was carried out on a Sun Sparc Classic UNIX-based workstation with the C^{++} programming language. The developed image processing system allows interactive filter design, convolution, spline positioning and editing, and optimization. The system allows the storing, retrieving, and printing of filters, snakes, and images. It provides measurement results both superimposed on the image and logged to disk.

A. Filter Construction

The parameters of (14)–(16) define the shape, and thereby the response of the S-Gabor filters. A series of filters with a characteristic width, σ_x, were constructed in order to determine the most appropriate filter for the anticipated vessel dimensions, approximately 0.5 to 5.0 mm for coronary arteries [36], [37]. Given a rough estimate of the resolution of the expected images of five pixels/mm, expected vessel dimensions within the images were on the order of 2.5 to 25 pixels. Fig. 7 shows the result of convolving a bank of Gabor filters with σ_x in the range 1–8 with lines of decreasing width (from 25 to three pixels) shown in profile. Note that only the smallest filter ($\sigma_x = 1$) enhances edges at the smallest scale, three pixels. Filters with $\sigma_x > 2$ identify the center of the 3-pixel line, rather than its edges. For this reason, all filters used in the

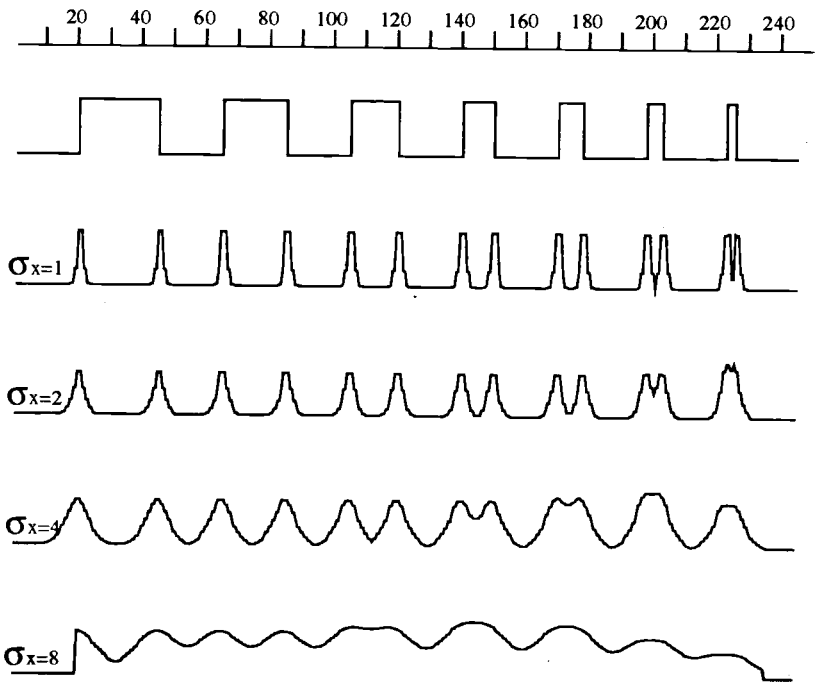

Fig. 7. S-Gabor filter response [energy, refer to (18)] for $\sigma_x = 1$ to 8 for the lines of decreasing width shown in profile at the top. The units displayed are pixels.

analysis of phantom and angiographic images were constructed with $\sigma_x = 1$.

Of the remaining parameters, k was arbitrarily set at 0.5, and v_0 was chosen such that $\sigma_x * v_0 = 0.39$. σ_y was chosen to yield a filter with orientation selectivity similar to natural vision systems: $\sigma_y = \sigma_x/0.5$ [30]. Finally, with all of the other parameters fixed, λ was determined numerically with bisection search to produce an even filter which integrated to zero (satisfying the desirable quality of zero dc response).

B. Feature Identification

Once an image had been filtered and the energy field constructed, the operator manually positioned the control points to draw two B-spline snakes close to the opposing vessel edges, spanning the region of interest. The snakes could be initialized with reference to the composite energy field, a user defined energy field built from any number of the available filter outputs, or the original (nonenhanced) image depending on which view afforded the best perspective. The number of piecewise cubic spans making up each snake could be increased or decreased at the discretion of the operator in order to best approximate the overall conformation of each vessel edge. Each snake was initialized by the operator in 15–30 s, depending on vessel complexity.

The splines were each independently optimized to the underlying composite energy field following the dynamic programming scheme discussed previously. Energy values between integer pixel locations in the energy field were calculated using bilinear interpolation. The total spline energy was calculated by numerically integrating the energy values along the length of the spline, and dividing by the length of the spline. Normalization of the total spline energy (with respect to length) eliminated the tendency for the snake to oscillate back and forth in space over a feature, decreasing energy solely by virtue of its increasing length. Each control point (with the exception of the end control points) was allowed to vary within a nine pixel window on each iteration. This nine pixel window confined possible control point positions to the current pixel and the eight nearest neighbors. For the analysis presented in this paper, the end points remained fixed in the location set by the operator when the spline was initialized, although the system does allow full movement of all control points. Fixing the end points prevented the possible migration of the spline away from, as well as extension of the spline beyond the region of interest. Fixing the end points reduced the time needed to converge on the optimum solution by reducing the total number of degrees of freedom of the system. Each snake converged on the optimal solution in 2–5 min on the Sun Sparc Classic workstation.

C. Vessel Measurement

Following optimization of the splines, characteristic measurements of the identified vessel were determined: minimum diameter, reference (normal) diameter, and percent-diameter stenosis. Only the overlapping sections of the two snakes were considered in the analysis. The minimum diameter and its location were found by searching for the shortest distance between the two splines within the overlapped region. Since the end points were fixed, the extent of the analysis along the vessel edges was determined exclusively by the operator, and did not reflect performance of the system. The beginning of the overlap at each end was defined by the shorter of the two shortest distances from the beginning of each snake to anywhere on the other.

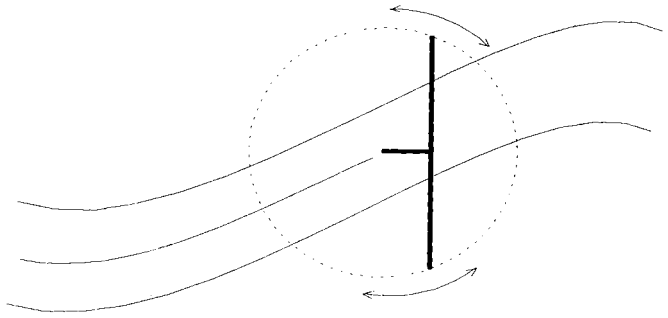

Fig. 8. Centerline calculation uses a rotating T-shaped construct. The orientation which results in equal length arms of the "T" defines the next point.

Vessel Centerline Construction: Next, the centerline falling between the two identified edges was calculated. Several different approaches have been used by other authors to construct the centerline. Gurley *et al.* [24] follow the contiguous path of lowest image energy corresponding to center of the vessel, a method similar to other skeletonizing schemes. Reiber *et al.* [39] start with a user-defined centerline and refine the estimate after the edges have been detected. Of note, both of these systems rely on the centerline as a reference from which to search for the vessel edge along perpendicular scanlines. In contrast, in the described algorithm the edges have already been detected and the centerline simply serves as a convenient construct from which to make measurements of vessel diameters.

In this analysis, centerlines were defined mathematically [27] as a line drawn between two edges such that, at any point along its length, its perpendiculars intersect the edges at equal distances from itself, and were constructed following the method of Bolson *et al.* [4], [5] which proceeds as follows. First, an estimate of the first point of the centerline is made. The midpoint of the line connecting the beginning points of the two splines within the overlapped region was chosen for convenience. Then, in an iterative process, new points along the centerline are sought using a T-shaped structure with long arms perpendicular to a short stem (see Fig. 8) which is anchored at its base to the last centerline point. The "T" is rotated and an orientation sought in which the two resulting distances along the arms to the edges are equal. The intersection of the stem and arms of the "T" then becomes the next point on the centerline. This process is repeated until the end of the overlapped region is reached.

D. Phantom Studies

Phantom studies were undertaken in order to validate the accuracy and precision of the system under ideal conditions. A Plexiglas precision-drilled, contrast-filled model and a series of flexible, contrast-filled tubes were imaged in the Yale New Haven Hospital (YNHH) digital catheterization lab and subsequently analyzed by a single operator.

A solid 1 cm $\times$ 10 cm $\times$ 10 cm plexiglas block was precision-drilled to yield a series of parallel holes with minimum diameters of 1.00, 1.50, 2.00, 3.00, 4.00, and 5.00 mm. Each hole was widened to 5.00 mm at each end to a depth of 1.5 cm to simulate normal pre- and post-stenotic vasculature. The modeled percent-diameter stenoses, therefore, ranged from 0–80%. These dimensions cover the range in size of normal and pathologic vessels commonly encountered in clinical practice, and have been used previously in other phantom experiments. The phantom was imaged with two of the stenotic sections centered in the image at a time with a window of 4.5 in at 75 keV, the standard energy level used in clinical procedures at YNHH, and filled with Hypaque-76 (Winthrop Pharmaceuticals, New York, NY) radiographic contrast.

Additionally, 1/32-in, 1/16-in, and 1/8-in inside diameter Tygon tubes were filled with Hypaque-76 and sealed at both ends. The tubes were taped to a solid surface in a randomly curved configuration and imaged along with the fixed-stenosis phantoms. The images were digitally recorded in short, 3–5 s bursts with automatic exposure control. Later, single frames from each of the phantom imaging runs were selected at random and transferred over local network to the Sun Classic workstation.

In the first validation series, a single operator filtered, initialized, and optimized the snakes for each of the phantoms at least four times, recording the resulting minimum and ninetieth-percentile diameters, percent-diameter stenosis and the shape and location of each optimized spline. In order to test the ability of the system to repeatably settle into the same spline configuration independent of the initial conditions, the 2-mm minimum diameter fixed-stenosis phantom was analyzed once, and the resulting optimized splines recorded as a standard reference; then, in ten independent trials, single or multiple control points were randomly displaced from their optimized reference locations, and the resulting splines recorded. The displaced splines were then reoptimized and their final position compared both to the displaced position and the original reference with regard to the minimum diameter, ninetieth-percentile diameter, percent-diameter stenosis, and the circumscribed area measure described earlier. This scheme was repeated for a single image of the 1/32-in ID tubing, as well.

E. Angiographic Studies

Angiograms of twenty coronary vascular lesions (including eight matched pre- and post-angioplasty lesions) were selected from eight sequential patients evaluated in the digital catheterization lab at YNHH. The images selected exhibit a range from normal to severely stenosed lesions, discrete to diffuse disease, and simple to complicated vessel geometries. Each image was analyzed independently by each of two operators twice with a washout period of several days between repeat analyzes. The resulting optimized splines were recorded; minimum diameter, ninetieth-percentile diameter, percent-diameter stenosis, and area circumscribed by each spline before and after optimization were calculated and recorded.

One angiogram was chosen to test the ability of the algorithm to repeatably settle into the same spline configuration regardless of the initial conditions in a manner identical to that described above for the phantom studies. This test was

TABLE I
ACCURACY AND PRECISION FOR FIXED-STENOSIS AND CURVED TUBE PHANTOMS

Phantom	Measure	90th-precentile diameter	minimum diameter	Percent-diameter stenosis
Fixed	accuracy	N/A	−0.14 mm	2.85%
	precision	N/A	0.07 mm	1.35%
Curved	accuracy	0.33 mm	−0.25 mm	12.18%
	precision	0.38 mm	0.13 mm	8.30%

TABLE II
ACCURACY AND PRECISION FOR TWO INDEPENDENT OPERATORS

Operator	Measure	90th-precentile diameter	minimum diameter	Percent-diameter stenosis
1	accuracy	−0.05 pixels	−0.31 pixels	−3.01%
	precision	0.89 pixels	0.54 pixels	5.80%
2	accuracy	0.86 pixels	−0.39 pixels	−5.07%
	precision	3.16 pixels	1.16 pixels	15.5 %

performed by a single operator and repeated ten times. Areas between the displaced splines and the reference spline, and between the optimized splines and the reference spline were recorded.

IV. RESULTS

A. Fixed-Stenosis Phantoms

The minimum diameter, and percent-diameter stenosis accuracy and precision of the system for the fixed-stenosis phantoms were calculated and are presented in Table I. The ninetieth-percentile diameter, which measured the diameter of the pre- or post-stenotic sections of the phantom (and had a true dimension of 5.00 mm for each phantom), was used to scale the minimum dimension for each phantom image.

Fig. 10 summarizes the optimization of the two snakes to the 2 mm minimum diameter phantom from initialization [Fig. 10(a)], through the 20 iterations required in this case for convergence. The snakes are shown after 5, 10, 15, and 20 iterations in Fig. 10(b)–(f). Fig. 10(f) shows the final optimized control point locations and snake conformation, and a line connecting the initial and final locations for each control point.

The sum of the areas between the two initialized and final optimized spline pairs for each run was calculated. This area is a reflection of the initial displacement of the splines from the final optimized locations. Chi-square analysis revealed a modest probability of association between error in minimum diameter stenosis and initial displacement ($\chi^2 = 5.03$, $0.05 > P > 0.01$). There was little probability of association between percent-diameter stenosis and initial displacement ($\chi^2 = 0.05$).

B. Curved Tube Phantoms

The accuracy and precision of the ninetieth-percentile diameter, minimum diameter, and mean diameter were calculated for the curved tube phantoms. The results are presented in Table I. The sum of the areas between the two initialized and optimized spline pairs for each run was calculated. Chi-square analysis revealed no probable associations between ninetieth-percentile diameter ($\chi^2 = 0.05$), minimum diameter ($\chi^2 = 0.14$), or percent-diameter stenosis ($\chi^2 = 0.19$) and initial displacement.

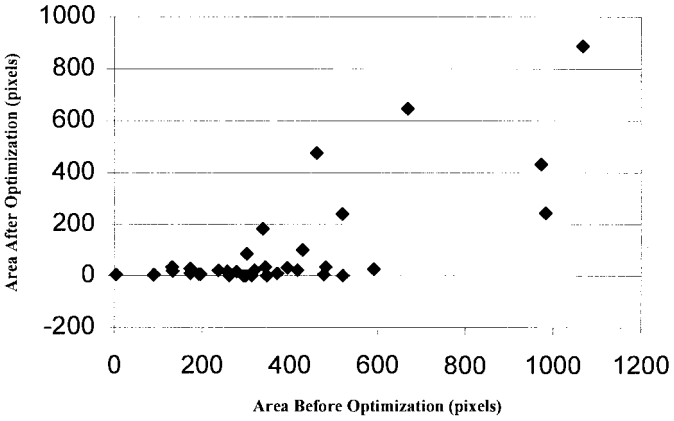

Fig. 9. Area between the initial reference spline and the displaced spline versus the area between the initial reference and the final optimized spline.

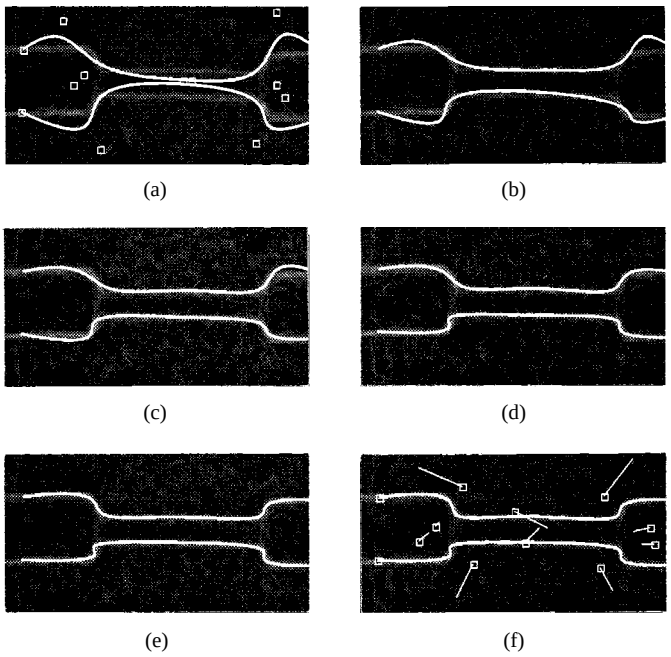

Fig. 10. Optimization of snakes on 2.00 mm fixed-stenosis phantom: (a) initialized, (b) after five iterations of DP algorithm, (c) after ten iterations, (d) after 15 iterations, (e) after 20 iterations, and (f) optimum reached at 23 iterations, lines connect initial control point locations and optimized locations.

C. Angiograms

Twenty coronary vascular lesions from nine sequential patients were analyzed with the algorithm. The series had a mean ninetieth-percentile diameter of 12.7 pixels, mean minimum diameter of 6.4 pixels, and mean percent-diameter stenosis of 49%. Figs. 11–13 show the results of the system on selected angiograms. These images demonstrate the robust behavior of the snakes, even in challenging situations. Accuracy and pre-

TABLE III
VARIABILITY AND MEAN DIFFERENCES COMPARING RUNS BY TWO INDEPENDENT OPERATORS

Measure	90th-precentile diameter	minimum diameter	Percent-diameter stenosis	Area between splines
Bias	0.38 pixels	−0.19 pixels	−3.79%	N/A
Variability	2.28 pixels	0.53 pixels	8.03%	N/A
Difference in means ±95% confidence limits	−0.91 ± 1.56 pixels	0.08 ± 0.61 pixels	2.06 ± 7.84%	−37.1 ± 47.1 pixels

cision measures were calculated for each of two operators and are presented in Table II. Bias between operators (the mean of the differences in mean measurements for each angiogram), variability between operators (the standard deviation of the differences in mean measurements for each angiogram) and differences and 95% confidence levels in the mean differences of ninetieth-percentile diameter, minimum diameter, percent-diameter stenosis between runs, and error in identified contours between runs (spline 1, run 1–spline 1, run 2; etc.) for each of the operators are presented in Table III. There were no significant differences between the means ($p > 0.05$) for any of the four quantities measured.

One image from the fixed-stenosis phantoms, one from the curved-tube phantoms, and one from the angiogram series were further analyzed to determine the repeatability of the algorithm under widely varying initial conditions. Splines were optimized on each of the images and recorded as a reference. Thereafter, one or more control points of one of the two splines were displaced and the spline reoptimized. Areas were calculated between the reference spline and the initially displaced spline position (averaging approximately 375 pixels), and between the reference spline and the resulting optimized spline (averaging approximately 100 pixels for all cases, but only 15 pixels when the optimization appeared to correctly reidentify the vessel border). Fig. 9 shows the results of these area calculations. Fig. 10 provides a subjective example of the magnitude of initial displacements which was typical for this analysis. Chi-square analysis of the pooled data revealed no probable association between initial and final areas ($\chi^2 = 0.53$).

V. DISCUSSION

A. Intraoperator Accuracy and Precision

Two phantom types were studied to measure the accuracy and precision of the vessel measurement system. The system exhibited better than pixel accuracy (1 pixel $\cong 0.16$ mm $\times 0.16$ mm) for minimum diameters for both the precision-drilled, fixed-stenosis and flexible-tube phantoms. The accuracy compares favorably with published results (Reiber, van der Zwet) summarized in Table IV.

While the precision was excellent for the fixed-stenosis phantoms, it was somewhat disappointing in the flexible tube phantoms with accuracies and precisions about half and twice those for the fixed-stenosis phantoms, respectively. This result is of dubious significance, however, considering true dimensions of the tubing along their lengths were unknown, confounded by possible squeezing or flattening in any number of places.

In the protocol described earlier, the operator was instructed to place the initialized splines "close" to the enhanced vessel edges. However, no strict definition of "close" was given, and it was up to the operator to interpret "closeness." In order to explore the relationship between initial closeness of the spline and the ultimate optimized shape, the area between the initialized spline and the optimized spline was calculated. This quantity was then correlated with the measurement error using chi-square analysis. Except in the case of minimum diameter error of fixed stenosis phantoms, there were no associations found between initial area and measurement error. The association found, however, was modest, and may be the result of chance. Thus, the error in measurement of vessel dimensions was independent of the initial distance away from the contour that the snake was placed.

B. Sources of Error

Several sources of error may be inherent in the vessel measuring algorithm and are important to identify in the interest of future system refinements. The first is that the S-Gabor filters do not consistently localize edges across different scales, i.e., at different widths of the Gaussian envelope, σ_x in (14) and (15). Nor is it likely that do they do so inherently accurately at any scale. As σ_x increases relative to the vessel being imaged, a point is reached at which the filter begins to see the vessel as a single line rather than as two edges (as the even filter begins to dominate the odd filter). To minimize this effect, we took $\sigma_x = 1$, making the S-Gabor filter system an edge detector for vessels of the scale being imaged. While the overall accuracy attained in the phantom studies was −0.14 mm, the precision was 0.07 mm. Thus the system underestimated the vessel minimum diameters on average, but did so in a very consistent fashion. Linear regression of true versus measured minimum diameter for the fixed-stenosis phantoms revealed a fixed offset of 0.08 mm such that $\min_{\text{true}} = \min_{\text{measured}} + 0.08$. This correction was independent of the measured mean dimension ($p < 0.01$).

A very important source of error involves the choice of the number of piecewise cubic spans used to construct the B-spline snake. The order of the spline spans (in this case, cubic) determines the possible spanwise conformation of the snake. Increasingly complex shapes can be mapped either by increasing the spanwise order of the B-spline function, or by increasing the number of spans. The latter method is the only practical solution, and the one that takes advantage of the efficiency of DP. When fitting initial curves "close" to the enhanced feature, using the developed image processing software the operator can add or subtract spans from the snakes as they see fit.

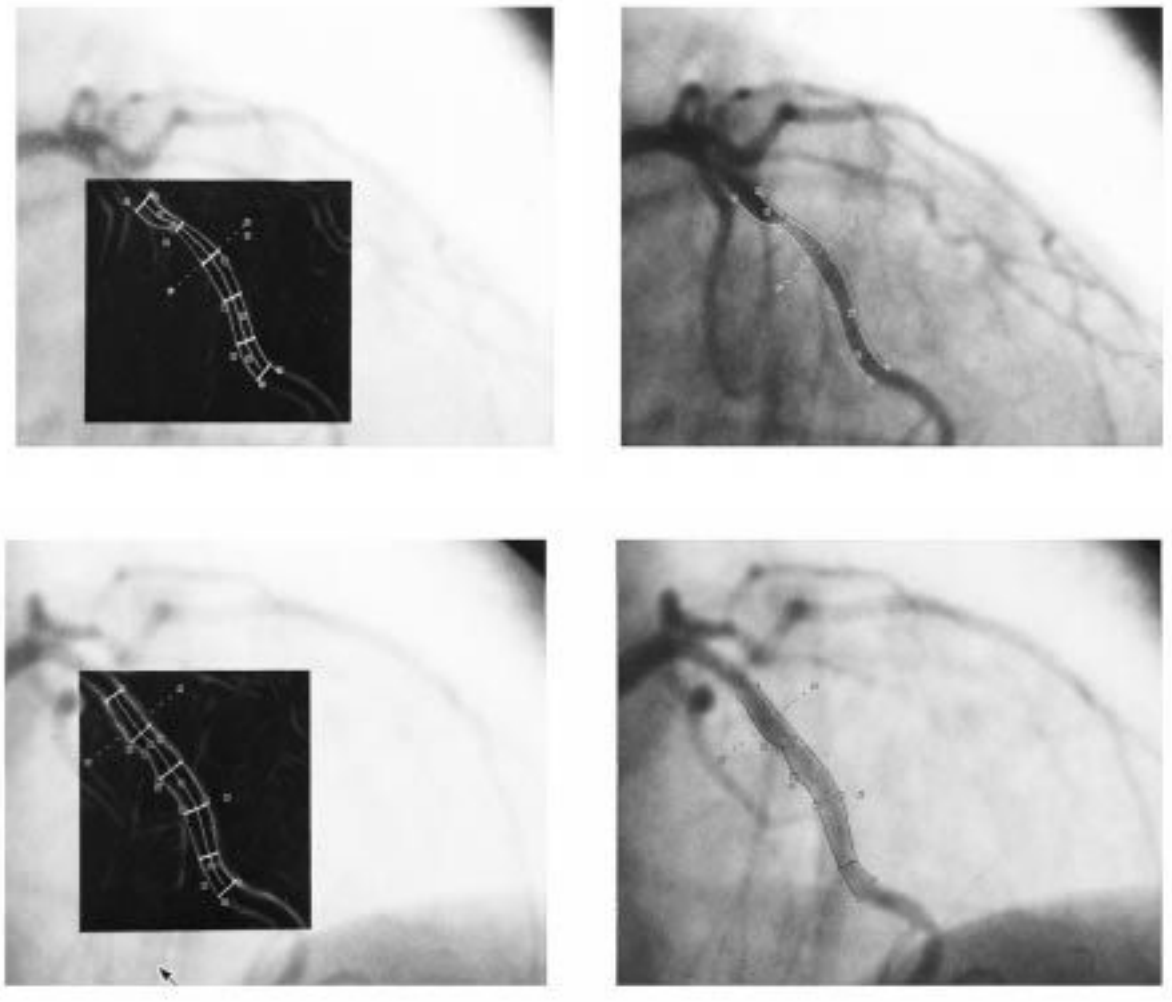

Fig. 11. Result of system operation on set of pre- and post-angioplasy images (top and bottom, respectively). Filtered regions are shown on left with splines (solid lines) and ninetieth-percentile diameter location (dashed line) superimposed. Note the small arteries which branch off within the region of interest. The system easily spans these discontinuities.

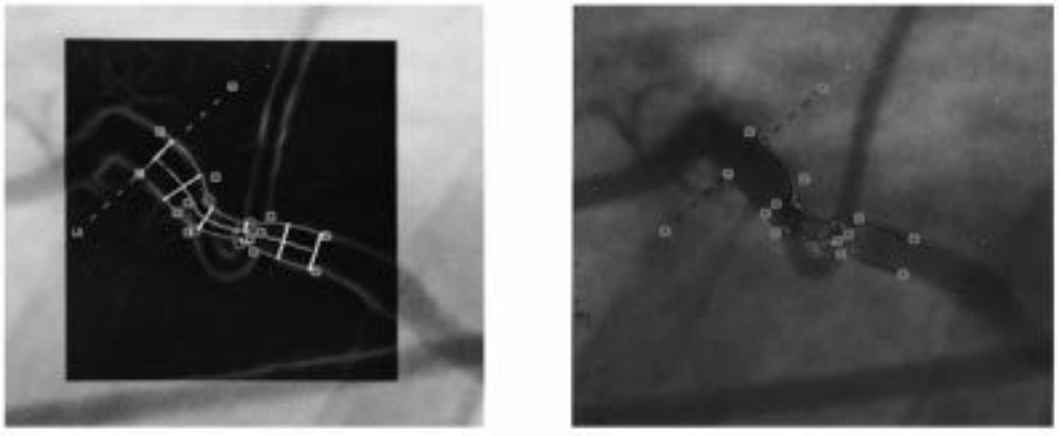

(a) (b)

Fig. 12. (a) Filtered region and (b) original angiogram with results of vessel border identification superimposed. Note the complexity of this lesion: a discrete narrowing bisected by an overlapping vessel.

Trying to match a feature with too few or too many spans leads to problems. When too few spans are specified, the optimized snake will understate the complexity of the vessel. This may lead to overstatement of minimum diameters, and understatement of reference diameters, especially in the case of diffuse disease. Specifying more spans than required to match the feature unnecessarily increases computation time for optimization. It may also, for unclear reasons, lead to

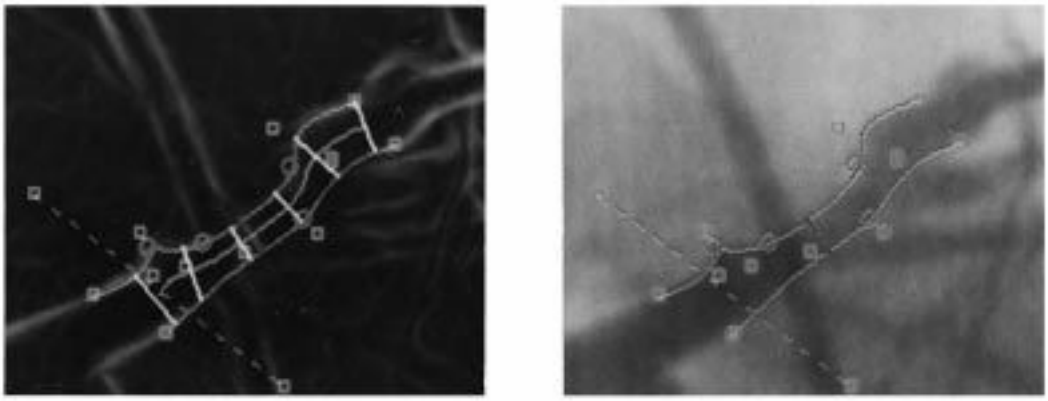

(a) (b)

Fig. 13. (a) Filtered region and (b) original angiogram with results of vessel border identification superimposed. Note the complexity of this lesion: multiple branching vessels, overlapping catheter, and sharp notch at the proximal end.

TABLE IV
SUMMARY OF QCA SYSTEM PERFORMANCE DESCRIBED IN LITERATURE

Author	Edge detection	Pixels/mm	Accuracy	Precision	Interoperator precision
Reiber [37]	Weighted 1st and 2nd difference	13.9	0.03 mm (0.42 pixel)*	0.09 mm (1.25 pixel)*	0.20 mm (2.78 pixel)*
van der Zwet [46]	Gradient field transform	13.9	0.06 mm (0.42 pixel)*	0.004 mm (1.58 pixel)*	0.14 mm (1.95 pixel)*

* approximate, based on reported image resolution.

optimization failures. It may be that the excessive number of spans gives the snake sufficient degrees of freedom to detour out and follow extraneous features and return to the remainder of the feature of interest. This was occasionally observed at vessel bifurcations or overlaps and in cases where the fixed starting or endpoints were incorrectly placed off to the side of the feature (rather than directly on it) allowing a loop of snake to slip past.

Another type of error occurs because there may be more than one locally optimal snake conformation in the region surrounding the best fit (globally optimal) conformation. The factor most likely to influence this result is the size of the window within which the DP algorithm moves the control points as it samples the various conformations. In all experiments described in this paper, the DP algorithm varied the control points within a nine pixel window. Increasing the window increases the total number of conformations examined by the DP algorithm and thus reduces the likelihood that the snake will settle into an isolated, nonglobally optimal solution. Increasing the window, however, comes at the expense of rapidly increasing computation time [from $\mathbf{O}(9^4)$–$\mathbf{O}(25^4)$, etc.].

Finally, the choice of reference diameter affects the accuracy and precision of the algorithm. In the analysis of the phantoms, the ninetieth-percentile diameter was assumed to represent the width of the nonstenosed phantom vessel segment. This was in turn used to scale the image dimensions to real world dimensions (each nonstenosed segment was drilled to 5.00 mm in diameter). Given that the ends of each spline were fixed in each of the experiments, it is conceivable that the ninetieth-percentile diameter may, in some cases, have depended more on the initial placement by the operator than by the results of the optimization. This would likely be the case if the endpoints were placed too widely, thus biasing the diameters toward an artificially large size.

C. Interoperator Bias and Variability

In order to deliver consistent, accurate results, a quantitative coronary angiography system should be as insensitive as possible to potential biases introduced by the operator. Measurements made by one operator should be consistent with measurements made by the same operator at some other time, as well as those by a different operator. In this analysis, a series of 20 coronary artery lesions from random angiograms of eight patients was analyzed by two independent operators twice in order to gauge the impact of operator bias. The interoperator bias, or the systematic difference in minimum diameter between the two operators was -0.19 pixels. The interoperator variability in minimum diameter measurement was 0.53 pixels, which compares very favorably with results reported by Reiber *et al.* (Table IV). There were no significant differences between the mean differences in the parameters measured (ninetieth-percentile diameter, minimum diameter, percent-diameter stenosis, and error areas) for operator 1 and the mean differences for operator 2. These results indicate that operator influence is minimal for the described system.

Of note, while the accuracy and precision in minimum diameter measurement were similar for the two operators, the same was not true for ninetieth-percentile diameter and percent-diameter stenosis measurements. The ninetieth-percentile diameter measurement depends heavily on the extents over which the system is applied. When analyzing a lesion, the operator must first choose the stenosis to span with the snakes, and then choose how far to match the vessel contours to either

side of the stenosis. The latter choice determines the possible range of reference diameters that can be selected by the system. The fact that the interoperator minimum-diameter variability was low indicates that the choice of stenoses was consistent between the operators. The greater interoperator variability and threefold difference in precision in ninetieth-percentile diameter, however, indicates that the choice of extents was not consistent. The threefold difference in percent-diameter stenosis variability is a direct consequence of the variability in ninetieth-percentile diameter.

The choice of the extent of the analysis is a difficult one and one that is clearly vulnerable to operator bias. Despite this, however, the accuracies in all three measured quantities were similar for both operators. Thus, while one operator exhibited wider variation in the extent of the lesion analysis, the end results, on average, were not as different as one might expect.

D. Robustness and Influence of Initial Conditions

The next step forward in the development of DQA systems will clearly be the advent of full automation and, thereby, the elimination of all operator bias in the measurement process. To date, all systems require some form of user initialization whether as a rough centerline estimate, end points, etc. Also, present systems exhibit high rates of failure (approaching 50% by some estimates [24]), especially when applied to complicated lesions such as occur in diffuse disease, or at branching or overlapping vessels. Systems which search a cost matrix to find the least-cost path from one end of a lesion to the other are vulnerable to following an incorrect path, especially in the cases cited.

A deformable vessel boundary model approach, such as the B-spline snake presented here, is less vulnerable to such failures as it can span complicated regions and then settle into the lowest energy state. Rather than begin at one point and follow a connected path to some other end point, snakes represent entire paths from starting point to end point. Optimization draws the snake into a conformation along that general path which minimizes the snake's energy and best fits the underlying edge contour.

Several of the experiments presented in this paper were designed to evaluate the ability of the algorithm to repeatably draw the deformable snake into the same optimal, minimum energy conformation, independent of the initial displacement away from that optimum. Phantom studies revealed no strong associations between the area circumscribed by the initial and optimal splines and variability in the measurements of ninetieth-percentile diameter, minimum diameter, or percent-diameter stenosis. Thus, the final result was insensitive to the initial spline placement which implies minimal operator introduced bias.

Another set of experiments performed on both phantoms and angiograms further tested the association between initial placement and optimized result. Two area measures (chosen to quantify the differences in spline locations along their entire extent) were compared. The first was the area circumscribed by an optimal reference spline and that same spline displaced some distance away. The second area was circumscribed by the reference spline and the result of optimizing the displaced spline. While no association between the two areas was found on the basis of chi-square analysis, the following observation should be noted. Optimization resulted either in a spline closely fitting the original reference, or it resulted in an entirely different result. There is no continuous range of final areas resulting from optimization: either the displaced splines converge on the initial reference splines, or they fail to locate the vessel edges catastrophically.

Locally optimal solutions may be encountered even in a random background. The spline algorithm appears to be more likely to encounter these false, locally optimal but globally-poor solutions the further the spline is displaced from the globally optimal solution. As stated earlier, increasing the size of the control point search windows would alleviate this problem.

ACKNOWLEDGMENT

The authors would like to thank R. Curwen, Ph.D. and J. Holihan, Ph.D., for help in the form of software, and statistical analysis. They would also like to thank K. Purushothoman, Ph.D. for his aid in construction of the phantoms, and G. Heyrich, M.D. for help in selecting and transferring images from the YNHH catheterization lab.

REFERENCES

[1] A. A. Amini, T. E. Weymouth, and R. C. Jain, "Using dynamic programming for solving variational problems in vision," *IEEE Trans. Pattern Anal. Machine Intell.*, vol. 12, no. 9, pp. 855–867, 1990.

[2] A. A. Amini, R. W. Curwen, and J. C. Gore, "Snakes and splines for tracking nonrigid heart motion," in *Lecture Notes in Computer Science*, vol. 1065, B. Buxton and R. Cipolla, Eds. Berlin, Germany: Springer-Verlag, Apr. 1996, pp. 251–261

[3] A. A. Amini *et al.*, "Physical models for measurement of blood velocity and flow from diagnostic images," in *Proc. Compters in Cardiology.* Piscataway, NJ: IEEE Computer Society Press, 1993, pp. 783–786.

[4] E. L. Bolson, S. Kliman, F. Sheehan, and H. T. Dodge, "Left ventricular segmental wall motion analysis—A new method using local direction information," in *Proc. Computers in Cardiology.* Piscataway, NJ: IEEE Computer Society Press, 1980.

[5] B. G. Brown, E. Bolson, M. Frimer, and H. T. Dodge, "Estimation of dimensions, hemodynamic resistance, and atheroma mass of coronary artery lesions using the arteriogram and digital computation," *Circ.*, vol. 55, no. 2, pp. 329–337, 1977.

[6] B. G. Brown, E. L. Bolson, and H. T. Dodge, "Arteriographic assessment of coronary atherosclerosis, review of current methods, their limitations, and clinical applications," *Arteriosclerosis*, vol. 2, no. 1, pp. 2–15, 1982.

[7] ———, "Quantitative computer techniques for analyzing coronary arteriograms," *Prog. Cardiovasc. Diseases*, vol. XXVIII, no. 6, pp. 403–418, 1986.

[8] I. Carlbom, D. Terzopoulos, and K. M. Harris, Computer-Assisted Registration, Segmentation, and 3-D Reconstruction from Images of Neuronal Tissue Sections, *IEEE Trans. Med. Imag.*, vol. 13, no. 2, pp. 351–362, Jun. 1994.

[9] D. M. Cavaye and R. A. White, "Imaging technologies in cardiovascular interventions," *J. Cardiovasc. Surg.*, vol. 34, no. 1, pp. 13–22, 1993.

[10] R. W. Curwen, A. A. Amini, J. S. Duncan, and F. Lee, "Tracking vascular motion in X-ray image sequences with Kalman snakes," in *Proc. Computers in Cardiology.* Piscataway, NJ: IEEE Computer Society Press, 1994, pp. 109–112.

[11] J. G. Daugman, "Two-dimensional spectral analysis of cortical receptive field profiles," *Vision Res.*, vol. 20, pp. 847–856, 1980.

[12] J. C. Daugman, "Six formal properties of two-dimensional anisotropic visual filters: Structural principles and frequency/orientation selectivity," *IEEE Trans. Syst., Man, Cybern.*, vol. SMC-13, no. 5, pp. 882–887, 1983.

[13] ——, "Uncertainty relation for resolution in space, spatial frequency, and orientation optimized by two-dimensional visual cortical filters," *J. Opt. Soc. Amer.*, vol. 2, no. 7, pp. 1160–69, 1985.
[14] T. A. DeRouen and J. A. Murray, "Variability in the analysis of coronary arteriograms," *Circ.*, vol. 55, no. 2, pp. 324–328, 1977.
[15] K. Doi *et al.*, "Digital radiography a useful clinical tool for computer-aided diagnosis by quantitative analysis of radiographic images," *Acta Radiologica*, vol. 34, no. 5, pp. 426–439, 1993.
[16] S. Ellis, W. Sanders, *et al.*, "Optimal detection of the progression of coronary artery disease: Comparison of methods suitable for risk factor intervention trials," *Circ.*, vol. 74, no. 6, pp. 1235–1242, 1986.
[17] M. A. T. Figueiredo and Leitô, "A nonsmoothing approach to the estimation of vessel contours in angiograms," *IEEE Trans. Med. Imag.*, vol. 14, no. 1, pp. 162–172, 1995.
[18] R. M. Flemming, G. M. Harrington, H. R. Gibbs, and J. Swafford, "Quantitative coronary arteriography and its assessment of atherosclerosis: Part I. Examining the independent variables," *Angiol.*, vol. 45, no. 10, pp. 829–833, 1994.
[19] ——, "Quantitative coronary arteriography and its assessment of atherosclerosis: Part II. Calculating stenosis flow reserve from percent diameter stenosis," *Angiol.*, vol. 45, no. 10, pp. 835–840, 1994.
[20] D. P. Foley *et al.*, "Quantitative coronary angiography (QCA) in interventional cardiology: Clinical application of QCA measurements," *Prog. Cardiovasc. Diseases*, vol. XXXVI, no. 5, pp. 363–384, 1994.
[21] G. G. Gensini, "Coronary arteriography," in *Heart Disease, A Textbook of Cardiovascular Medicine*, E. Braunwald, Ed. Philadelphia: Saunders, 1980.
[22] K. L. Gould, "Quantification of coronary artery stenosis *in vivo*," *Circ. Res.*, vol. 57, no. 3, pp. 341–353, 1985.
[23] K. L. Gould, K. O. Kelley, and E. L. Bolson, "Experimental validation of quantitative coronary arteriography for determining pressure-flow characteristics of coronary stenosis," *Circ.*, vol. 66, no. 5, pp. 930–937, 1982.
[24] J. C. Gurley, S. E. Nissen, D. C. Booth, and A. DeMaria, "Influence of operator- and patient-dependent variables on the suitability of automated quantitative coronary arteriography for routine clinical use," *J. Amer. College Cardiol.y*, vol. 19, no. 6, pp. 1237–1243, 1992.
[25] D. G. Harrison *et al.*, "The value of lesion cross-sectional area determined by quantitative coronary angiography in assessing the physiologic significance of proximal left anterior descending coronary arterial stenoses," *Circ.*, vol. 69, no. 6, pp. 1111–1119, 1984.
[26] F. Heitger, L. Rosenthaler, R. von der Heydt, E. Peterhans, and O. Kubler, "Simulation of neural contour mechanisms: From simple to end-stopped cells," *Vision Res.*, vol. 32, no. 5, pp. 963–981, 1992.
[27] G. James and R. C. James, Ed., *The Mathematics Dictionary.* Princeton, NJ: Van Nostrand, 1968.
[28] M. Kass, A. Witkin, and D. Terzopoulos, "Snakes: Active contour models," *Int. J. Comput. Vision*, vol. 1, no. 4, pp. 121–131, 1988.
[29] A. Klein, "Implementation and Validation of a Quantitative Coronary Angiography System," M.D. thesis, Yale Univ. School of Med., New Haven, CT, 1995.
[30] J. J. Kulikowski, S. Marcelja, and P. O. Bishop, "Theory of spatial position and spacial frequency relations in the receptive fields of simple cells in the visual cortex," *Biological Cybern.*, vol. 43, pp. 187–198, 1982.
[31] W. J. Mack *et al.*, "Comparison of computer- and human-derived coronary angiographic end-point measures for controlled therapy trials," *Arteriosclerosis, Thrombosis*, vol. 12, no. 3, pp. 348–356, 1992.
[32] G. B. J. Mancini *et al.*, "Automated quantitative coronary arteriography: Morphologic and physiologic validation *in vivo* of a rapid digital angiographic method," *Circ.*, vol. 75, no. 2, pp. 452–460, 1987.
[33] M. L. Marcus *et al.*, "Visual estimates of percent diameter coronary stenosis: A battered gold standard," *J. Amer. College Cardiol.*, vol. 11, no. 4, pp. 882–885, 1988.
[34] S. Menet, P. Saint-Marc, and G. Medioni, "B-snakes: Implementaion and application to stereo," in *Proc. 3rd Int. Conf. Computer Vision*, 1990, pp. 720–726.
[35] M. C. Morrone and D. C. Burr, "Feature detection in human vision: A phase-dependent energy model,"*Proc. R. Soc. Lond. B*, vol. 235, pp. 221–245, 1988.
[36] K. Reagan, L. M. Boxt, and J. Katz, "Introduction to coronary arteriography," *Radiological Clinics of North America*, vol. 32, no. 3, pp. 419–433, 1994.
[37] J. H. C. Reiber and P. W. Serruys, "Quantitative coronary angiography," *Cardiac Imaging—A Companion to Braunwald's Heart Disease*, M.L. Marcus, *et al.*, Eds. Philadelphia: Saunders, 1991.
[38] J. H. C. Reiber, P. W. Serruys, *et al.*, "Assessment of short-, medium-, and long-term variations in arterial dimensions from computer-assisted quantitation of coronary cineangiograms," *Circ.*, vol. 71, no. 2, pp. 280–288, 1985.
[39] J. H. C. Reiber, C. J. Kooijman, *et al.*, "Coronary artery dimensions from cineangiograms—Methodology and validation of a computer-assisted analysis procedure," *IEEE Trans. Med. Imag.*, vol. MI-3, no. 3 pp. 131–140, 1984.
[40] B. J. Rensing *et al.*, "Which angiographic variable best describes functional status 6 months after successful single-vessel coronary balloon angioplasty?," *J. Amer. College Cardiol.*, vol. 21, no. 2, pp. 317–324, 1993.
[41] L. Rosenthaler, F. Heitger, O. Kubler, and R. von der Heydt, "Detection of general edges and keypoints," *Proc. of European Conference on Computer Vision.* Berlin, Germany: Springer Verlag, 1992.
[42] B. G. Schunck, *Gaussian Filters and Edge Detection.* Warren, MI: General Motors Research Laboratories—5586, 1986.
[43] M. Sonka, M. D. Winniford, and S. M. Collins, "Robust simultaneous detection of coronary borders in complex images," *IEEE Trans. Med. Imag.*, vol. 14, no. 1 pp. 151–161, 1995.
[44] L. H. Staib and J. S. Duncan, "Boundary finding with parametrically deformable models," *IEEE Trans. Pattern Anal. Machine Intell.*, vol. 14, no. 11, pp. 1061–1075, 1992.
[45] B. H. Strauss *et al.*, "Technologic considerations and practical limitations in the use of quantitative angiography during percutaneous coronary recanalization," *Progress Cardiovasc. Diseases*, vol. XXXVI, no. 5, pp. 343–362, 1994.
[46] P. M. J. van der Zwet and J. H. C. Reiber, "A new algorithm to detect irregular coronary boundaries: The gradient field transform," in *Proc. Comput. in Cardiol.*, 1992.
[47] ——, "A new approach for the quantification of complex lesion morphology: The gradient field transform; basic principles and validation of results," *J. Amer. College Cardiol.*, vol. 24, no. 1, pp. 216–224, 1994.
[48] C. W. White *et al.*, "Does visual interpretation of the coronary arteriogram predict the physiologic importance of a coronary stenosis?," *New Eng. J. Med.*, vol. 310, no. 13, pp. 819–824, 1984.
[49] R. F. Wilson, M. L. Marcus, and C. W. White, "Prediction of the physiologic significance of coronary arterial lesions by quantitative lesion geometry in patients with limited coronary artery disease," *Circ.*, vol. 75, no. 4, pp. 723–732, 1987.
[50] W.-H. Wong, R. L. Kirkeeide, and K. L. Gould, "Computer applications in angiography," in *Cardiac Imaging and Image Processing*, Collins and Skorton, Eds. New York: McGraw-Hill, 1986, pp. 206–237.
[51] A. Yuille, D. Cohen, and P. Hallinan, "Facial feature extraction by deformable templates," Harvard Robotics Lab, Cambridge, MA, Tech. Rep. 88-2, 1988.
[52] L. M. Zir, S. W. Miller, R. E. Dinsmore, J. P. Gilbert, and J. W. Harthorne, "Interobserver variability in coronary angiography," *Circ.*, vol. 53, no. 4, pp. 627–676, 1976.